Image guided surgery: clinical validation of lesion identification technologies and exploration of nerve sparing approaches

KleinJan, G.H.

Citation

KleinJan, G. H. (2018, March 8). *Image guided surgery: clinical validation of lesion identification technologies and exploration of nerve sparing approaches*. Retrieved from https://hdl.handle.net/1887/61007

Note: To cite this publication please use the final published version (if applicable).

Cover Page

Universiteit Leiden

The following handle holds various files of this Leiden University dissertation:
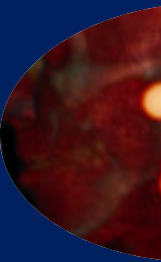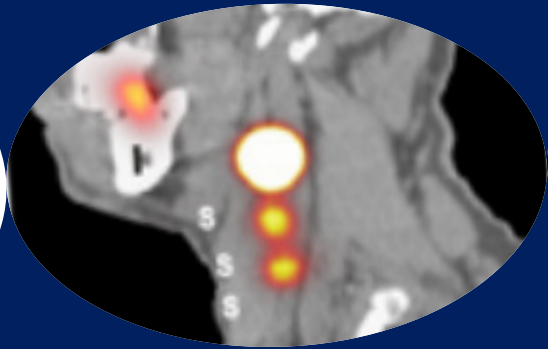http://hdl.handle.net/1887/61007

Author: KleinJan, G.H.
Title: Image guided surgery: clinical validation of lesion identification technologies and exploration of nerve sparing approaches
Issue Date: 2018-03-08
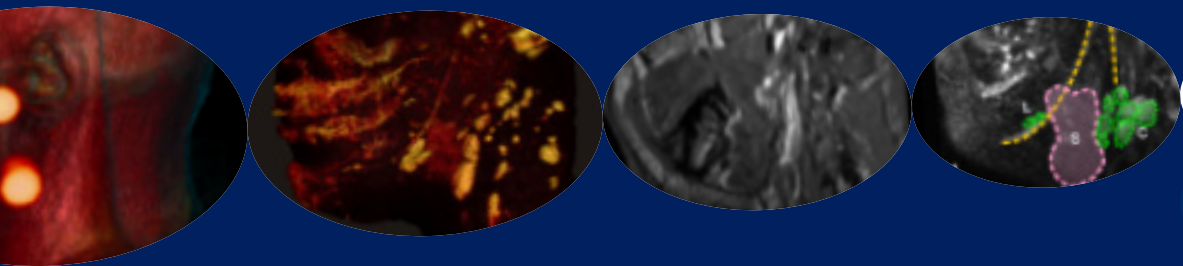
Chapter 11

Diffusion-weighted-preparation (D-prep) MRI as a future extension of SPECT/CT based surgical planning for sentinel node procedures in the head-and-neck area?

Tessa Buckle
Gijs H. KleinJan
Thijs Engelen
Nynke S. van den Berg
Marco C. DeRuiter
Ulke van der Heide
Renato A. Valdés Olmos
Andrew Webb
Marc A. van Buchem
Alfons J. Balm
Fijs WB van Leeuwen

11

ABSTRACT

INTRODUCTION
Even when guided by SPECT/CT-based surgical planning of nodal resections in the head-and-neck area is challenging due to the many critical anatomical structures present within the surgical field. In this chapter the potential of a (SPECT/)MRI-based surgical planning method was explored. Hereby MRI increases the identification of SNs within clustered lymph nodes (LNs) and vital structures located adjacent to the SN (such as cranial nerve branches).

METHODS
SPECT/CT and pathology reports from 100 head-and-neck melanoma and 40 oral cavity cancer patients were retrospectively assessed for SN locations in levels I-V and degree of nodal clustering. A diffusion-weighted-preparation magnetic resonance neurography (MRN) sequence was used in eight healthy volunteers to detect LNs and peripheral nerves.

RESULTS
In 15% of patients clustered nodes were retrospectively shown to be present at the location where the SN was identified on SPECT/CT (level IIA: 37.2%, level IIB: 21.6% and level III: 15.5%). With MRN, improved LN delineation enabled discrimination of individual LNs within a cluster. Uniquely, this MRI technology also provided insight in LN distribution (23.2±4 LNs per subject) and size (range 21-372 mm^3), and enabled non-invasive assessment of anatomical variances in the location of the LNs and facial nerves.

CONCLUSION
Diffusion-weighted-preparation MRN enabled improved delineation of LNs and their surrounding delicate anatomical structures in the areas that most often harbor SNs in the head-and-neck. A combined SPECT/MRI approach is envisioned for future surgical planning of complex SN resections in this region.

INTRODUCTION

Sentinel node (SN) biopsy procedures are a common example of an approach routinely performed using image guidance [1-2]. In a state-of-the-art setting pre-operative single photon computed tomography combined with computed tomography (SPECT/CT) images is used to define the number and location of the SNs (using the nuclear component) and their general location (using the CT component; Scheme 1A). However, even with careful preoperative planning, in general 3-10% of patients that undergo lymph node (LN) biopsy in the neck show iatrogenic nerve damage-related side effects (e.g. persistent pain in neck and shoulder area) and long-term postoperative side-effects such as sensory disturbance are even more common (65%) [3].

Previous evaluation of SN biopsy procedures performed in the head-and-neck region revealed that in 8-19% of patients clustered nodes (clusters are defined as two or more nodes that lie in direct proximity/contact to each other) provide a challenge during surgery. Due to the relatively poor spatial resolution and limited anatomical soft-tissue contrast of SPECT/CT, identification of the true SN within a cluster of LNs can be considered challenging. This often results in the requirement to expand surgical exploration based on intraoperative nodal findings and can increase the chance of surgical side-effects when performed in the vicinity of vital structures in the neck. In the case of incomplete SN resection, meaning not all the positive nodes within such a cluster are removed, this may provide false-negative results [4-7].

Diagnostic CT (170 mA, 120 kV) has a much higher resolution than the routinely used low-dose CT (40mA, 130 kV) and its use could thereby inherently result in improved SPECT/CT-based delineation and discrimination of LNs. However, in our clinic, the corresponding high-dose radiation exposure is considered undesirable for the diagnostic SN biopsy procedure. Magnetic resonance (MR) imaging (MRI)) is already part of the standard diagnostic work-up in head-and-neck cancer and has the possibility to provide a no-ionizing dose, high-resolution alternative to CT [8]. This is especially interesting when one considers that, depending on the imaging sequence used, MRI can provide unique types of soft-tissue contrast [9, 10]. For example, diffusion-weighted preparation (D-prep) MR neurography (MRN), which integrates a T2-weighted (spin-echo) preparation module, with diffusion weighted imaging and fat suppression can be used to identify nerve structures [11].

By combining the preoperative need for nodal cluster identification and peripheral nerve visualization it was reasoned that the implementation of MRI (T1 and D-prep MRN) into the planning of SN biopsy procedures could help improve the anatomical information provided

11
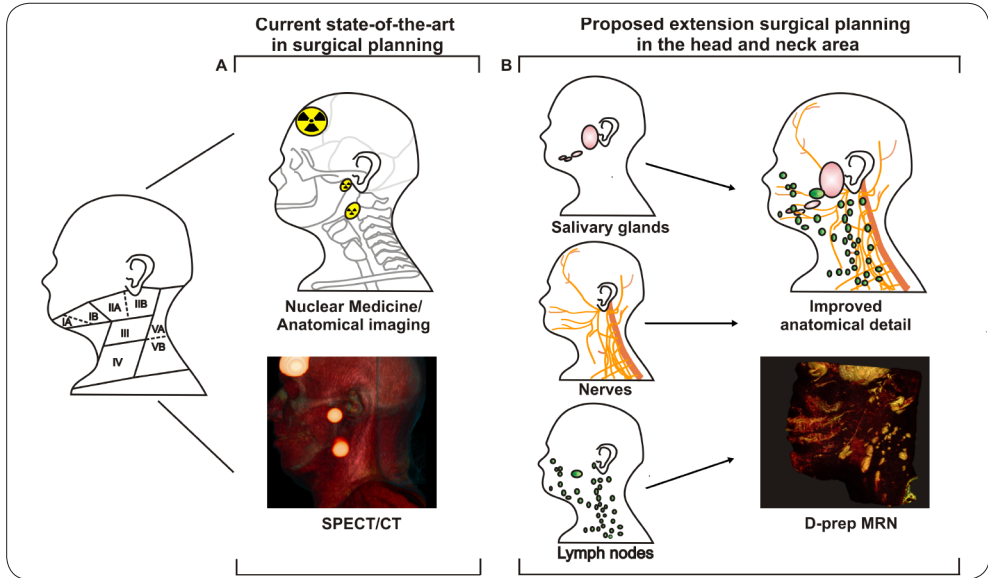
Scheme 1. Virtual surgical planning for SN biopsy procedures the head-and-neck area.

A) SPECT/CT provides the ability to localize SNs within their density-based anatomical context (neck level I-V), B) A proposed extension of the virtual planning concept using diffusion-weighted-preparation (D-prep) MRN to accurately delineate LNs and define their position relative to delicate anatomical structures such as peripheral nerves.

by SPECT/CT (Scheme 1B). To study the possible value of such an approach, first SPECT/CT results, surgical findings and pathology reports from 140 patients that underwent an SN biopsy procedure for head-and-neck or oral cavity malignancies were retrospectively assessed. This information was used to assess which area of the neck would benefit most from more detailed imaging evaluation. As clinical evaluation would require adaptation of the current clinical routine, the potential of D-prep MRN in the detection of peripheral nerves but also LNs and their distribution was first assessed in a pilot feasibility study in eight healthy volunteers. Together these findings allow for speculation on the value of D-prep MRN for future SN biopsy procedures.

MATERIAL AND METHODS

Patients and volunteers

Pre- and intraoperative imaging results and pathology reports from 100 head-and-neck melanoma and 40 oral cavity cancer patients who underwent SN biopsy between 2011-2014 using the hybrid tracer indocyanine green-^{99m}Tc-nanocolloid were assessed in retrospect. Patients included in this database were, in part, previously included in other clinical studies focused on image-guided removal of the SNs [5,13-15].

Eight healthy volunteers were prospectively included after obtaining written informed consent. The study was approved by the Scientific Committee of the Department of Radiology at the LUMC and all procedures were performed in accordance with the ethical standards of the institutional research committee and with the 1964 Helsinki declaration and its later amendments or comparable ethical standards.

SN biopsy procedure

Tracer injection and preoperative SN mapping was performed as previously described [4, 12]. In brief, a total of 0.4 mL hybrid tracer was injected surrounding the primary tumor lesion or the melanoma scar. Thereafter lymphoscintigraphy and SPECT and CT (40 mAs, 130 kV, 2 mm slices) imaging was performed. After reconstruction, SPECT and CT images were fused using Osirix Medical imaging software (Pixmeo, Geneva, Switzerland) and 3D volume-rendered SPECT/CT images (Osirix) were generated. The nuclear medicine physician determined the number and location of SNs based on the preoperative imaging dataset. The SN was defined as a LN receiving direct drainage from the primary tumor site [6]. The SN location was indicated on SPECT/CT according to the American Joint Committee on Cancer

AJCC)-Union for International Cancer Control (UICC) TNM staging system which distingue seven lymph node levels in each side of the neck [13].

Intraoperatively SNs were identified at the neck levels indicated by SPECT/CT using a combination of gamma imaging, gamma tracing and fluorescence imaging [4,12]. Histopathology was performed to determine whether or not the excised nodes contained (micro-) metastasis.

SN biopsy database analysis
A nodal cluster was defined as a hotspot identified on SPECT that contained several components or a diffuse pattern on CT. Clustered LNs were identified via retrospective analysis of the CT images i) when intraoperative SN identification via fluorescence imaging or gamma tracing/imaging revealed multiple nodes at the same location, [4] and ii) when during pathological evaluation excised specimen multiple nodes were identified by the pathologist.
The percentage of nodal clusters, and the incidence of SN identification per level (I-V), and the percentage of tumor-positive SNs were calculated using the following equations:

Eq. 1) Percentage of nodal clusters per level: ((number of clusters per level)/(total number of CT-identified clusters level I-V))*100%;

Eq. 2) Percentage incidence of SNs per neck level: ((number of SNs per level)/(total number of excised SNs level I-V))*100%;

Eq. 3) Percentage of tumor-positive SNs: ((number of SNs with metastasis)/(total number of excised SNs level I-V))*100%.

MRI in healthy volunteers
D-prep MRN was performed on a Philips 3T Ingenia MRI system in eight healthy volunteers using a slightly altered version of the D-Prep MRN sequence described by Yoneyama et al [11], with a spin-echo module (TE: 52 ms) and a spatially adiabatic inversion recovery (SPAIR)-based fat suppression (voxel size: 1.09x1.09x0.899 mm) using an eight-channel receive only head coil. Scanning time was approximately five minutes for a field of view (FOV) that comprised level I-V and two-to-three minutes for a FOV that comprised the submandibular region (level I-III). Sagittal images were acquired for both different sequences. Evaluation of

the location of the different levels within the D-prep MRN images was performed using side-by-side comparison with anatomical reference images of the same field of view (acquired using a standard clinical T1-3D turbo spin echo (TSE) sequence).

MR image analysis

Maximum intensity projection (MIP) images (max 10 slices) and overlays of both MR images were made using Osirix Medical imaging software (Pixmeo).

For assessment of the anatomical variances that can influence the risk of nerve damage during the SN biopsy procedure the diameter and location of the facial nerves were determined. On top the diameter and width of the LNs were measured. Finally the range in distance between the nerves and LNs located within level I-V and the nerves or LNs in relation to the submandibular salivary gland were determined. All measurements were performed using the measuring tool in the Osirix Medical imaging software package (Pixmeo).

To determine the (smallest) nerve diameter that could be visualized, three different measurements along the course of the nerves were taken. Here it must be noted that sections with a diameter of <0.7 mm could not be accurately assessed and were therefore not taken into account. To provide a quantitative measure for the risk of nerve damage during nodal dissection the distance between facial nerves, the closest LN and the submandibular salivary gland was measured (in triplicate). In all measurements the reproducibility between observers was determined by calculating the average and standard deviation (SD) for each measurement.

The distribution of the LNs over level I-V was evaluated by determining the number and size of LNs located in each level. Volumetric assessment of the size of the LNs and nodal clusters was conducted as previously described using the Cavalieri principle [14]. As such for assessment of ellipsoid shapes the following equation was used:

Eq. 4) LN volume: $(3/4\pi) \times (1/2a) \times (1/2b) \times (1/2c)$.

11

Here a and b represent the measured width (short axis) of the LN or cluster and c represents the diameter of the LN (long axis).

RESULTS

Retrospective assessment of cluster incidence and location within level I-V based on preoperative SPECT/CT imaging

Retrospective assessment of SPECT/CT scans, intraoperative imaging data and pathology results, which contained level I-V of the 140 included patients (Scheme 1), revealed that in 15% of patients more than one LN was found at the location of the hotspot that was identified as the SN on SPECT/CT (Figure 1 for nodal cluster distribution and Figure SI1D for an overview of SN localization). Re-assessment of the preoperatively obtained low-dose CT images resulted in the identification of some of the LN clusters (53; Figure 1A), but did not allow for in the identification of the exact number of SN within these LN clusters. For additional information on preoperative identification of SNs using SPECT/CT imaging (Figure SI1 shows a typical example), and surgical and pathological findings, see the supporting information (SI) section. Combined these findings suggest that the highest number of SN clusters and tumor-positive SNs are encountered in level II (Figure 1).

MRI-based evaluation of LN distribution in level I-V

MRI-based efforts on improving the preoperative imaging for the planning of minimally-invasive surgery were first also focused on level I-V. The D-prep MRN sequence used was originally designed for nerve visualization, based on the diffusion properties the nerve. As the diffusion properties of LNs are thought to be comparable to those of nerves, it is therefore not surprising that the use of this sequence also allowed visualization of LNs; LNs within level I-V of the healthy volunteers studied could be clearly delineated (Figure 2; scan time approximately five minutes). Not only were individual LNs visualized, discrimination could also be made between LNs located in clusters of three to five nodes (Figure 2).

Comparison of the images obtained in the eight different volunteers revealed a clear intra-volunteer variation in the distribution and number of LNs over the levels (see Figure 2, LNs highlighted in green) (as demonstrated in Scheme 1). On average 2±3 LNs were identified within level I-V (range: 1-11 LNs per level). An average number of nine, six and five LNs were detected per subject in level IIA, IIB and III respectively. Only a small number of nodes were detected in level I, IV or V (average of 1-4 nodes per level). For differences in sizes between individual LNs and LN clusters, see SI.
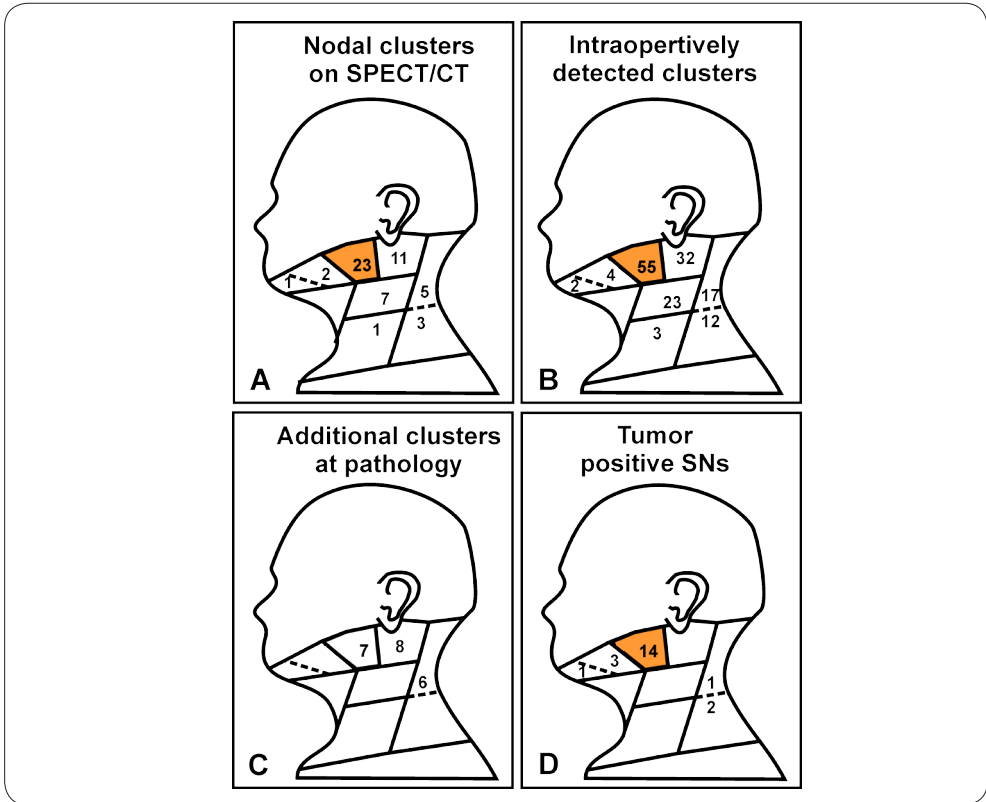
Figure 1. Incidence and location of LN clusters and metastases.

A) Amount of nodal clusters detected in level I-V (See Scheme 1) using preoperative SPECT/CT imaging:

B) Intraoperatively identified nodal clusters;

C) Additional nodal clusters identified at pathology;

D) Pathologically identified metastases. In orange, the level with the highest incidence of clustered nodes or nodal metastasis. Also see the supporting information for additional information on preoperative identification of SNs using SPECT/CT imaging and surgical and pathological findings.
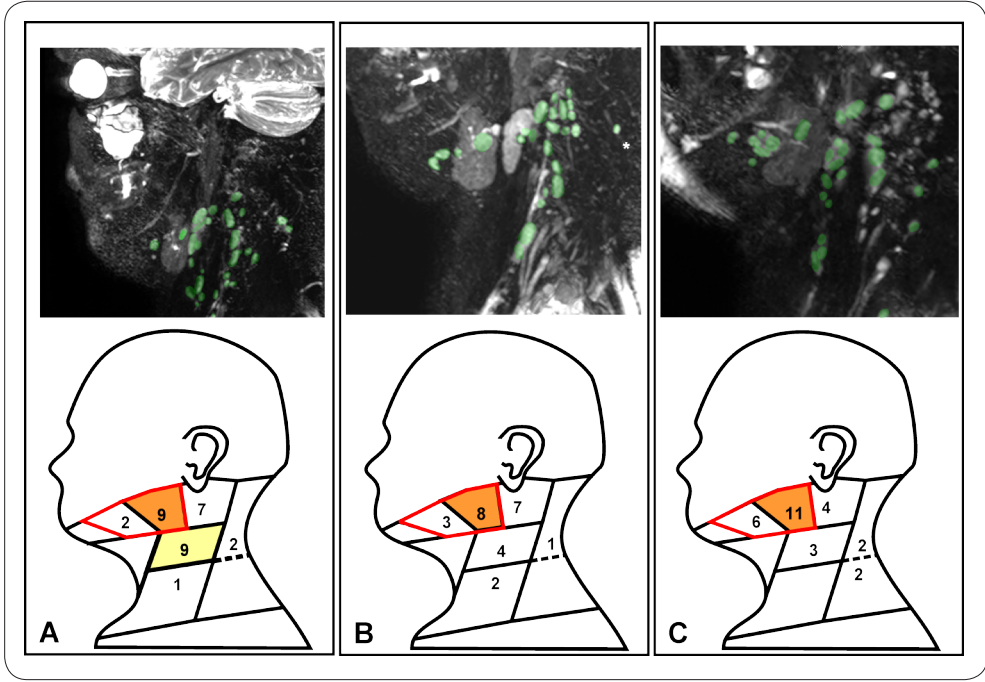
Figure 2. Variation in LN distribution within level I-V.

MRN images of the distribution of LNs in three different subjects (A-C) with stratification of LNs (highlighted in green) in level I-V (MIP of one side of the neck; scan time approximately five minutes). The level with the highest amount of visualized LNs is highlighted in orange, or in case of detection of the same amount of LNs in two different levels, in orange and yellow. Levels where the smallest LNs were found are traced in red.

MR-based imaging of the nerves in the submandibular region (including level II)

As both the highest number of SNs (Figure 1) and LNs (Figure 2) were shown to be located in level II further efforts on the improvement of the detail of preoperative imaging were focused on the submandibular region, which intricate anatomy includes level II (Figure 3A; FOV traced in red). Images of this FOV obtained with standard T1 3D TSE imaging (Figure 3; i) and D-prep MRN (Figure 3; ii en iii) resulted in the visualization of different anatomical features. Standard T1 3D TSE-based imaging did not result in clear LN delineation, but provided clear visualization of the blood vessels (Figure 3; i). With the D-prep MRN sequence these blood flow-related signals were suppressed. Combined with fat suppression, this resulted in visualization of nerve structures (Figure 3; ii).

Anatomical variances

To determine if it was possible to provide a measure for the chance of damage to delicate peripheral nerves during the resection of LNs in the head-and-neck area, distances between the LNs and the nearby nerves were recorded (Table 2). The highlighted representation of the structures visualized using D-prep MRN shown in Figure 3iii demonstrate the close relation between the location of the visualized LNs (in green), nerves (in yellow) and the submandibular salivary gland (in pink). An example of how close this relationship can be, is demonstrated in Figure 3B, which shows a cluster of three nodes that are located between and in close proximity to a facial nerve and the submandibular salivary gland.

Overall the distance between the node located closest to the nerve and the nerve itself ranged from 0.9 mm to 6.2 mm. The measured distances varied strongly between subjects. For example, the distance measured in the subject depicted in Figure 3B (1.8±0.80 mm) was three times smaller than the distance measured in the subject depicted in Figure 3C (6.2±0.1 mm). In the subject depicted in Figure 3Ciii one LN (L) was found to be located directly on top of the nerve, while in the subject depicted in Figure 3Diii a individual node as well as a cluster of nodes was found to be directly overlaying the nerve (Table 1). In such cases resection without inducement of nerve damage may be complex. For additional observations on structures of interest (Table 1) and anatomical variances, e.g. between the position of the facial nerve and the submandibular salivary gland, see SI.
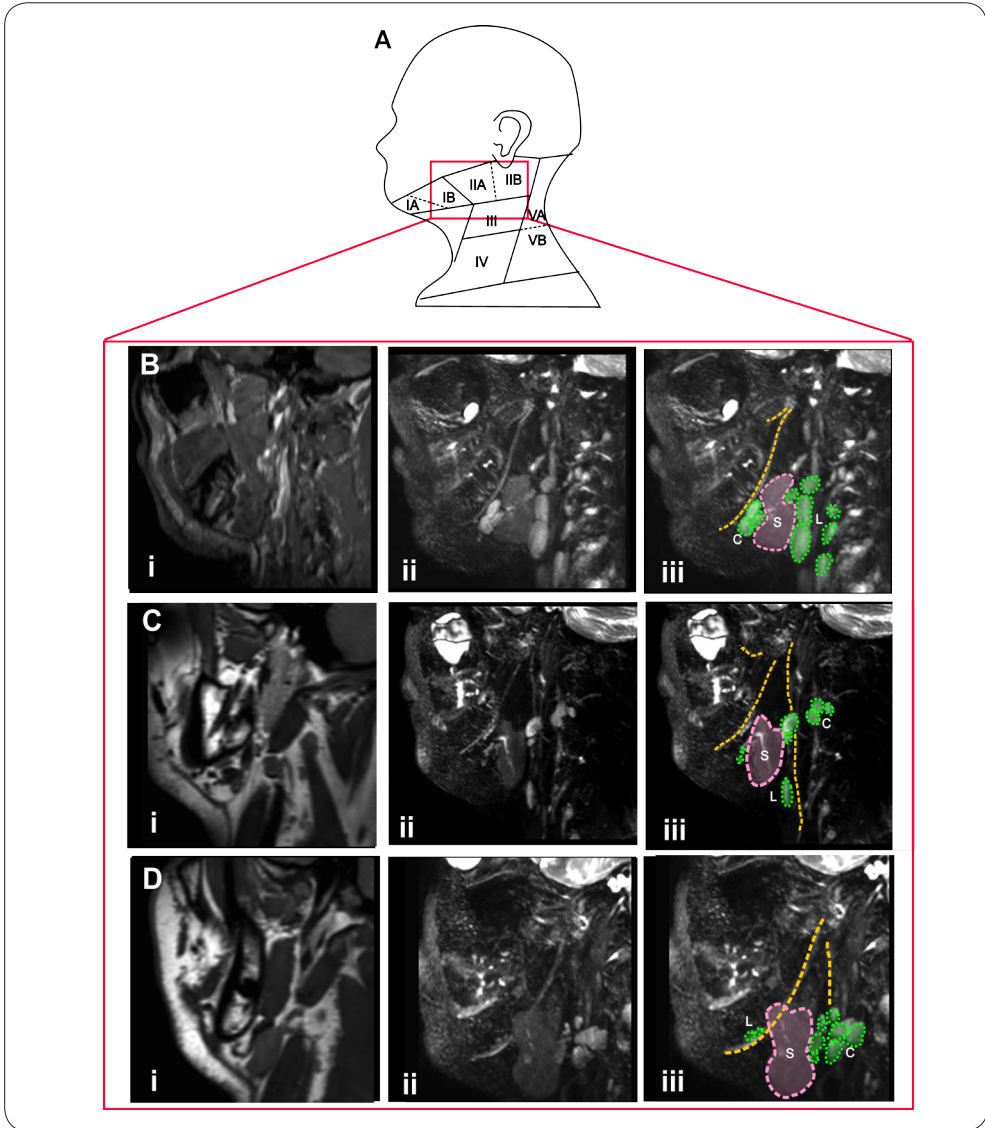
11

Figure 3. MR-based imaging of the submandibular region.

A) Schematic representation of the FOV, which includes level II (in red). B-D) MR images of different healthy volunteers obtained with i) standard T1-3D TSE (single slice) and ii) D-prep MRN (MIP, 10 slices. Scan time two-three minutes). iii) D-Prep MRN images of the same subject wherein visualized structures are traced and highlighted. Here LNs are depicted in green, nerves in yellow and the submandibular salivary gland in pink. Individual LNs = L, LN clusters = C and the submandibular salivary gland = S.

- Structures of interest	- Number of subjects in which structure is identified	- Range in distance between structures (mm)
- LN/ nerves	- 8/8	
- LN adjacent to nerve	- 8/8	- 0.9 – 6.2
- LN on top of nerve	- 1/8	- n.d.*
- Nerve alongside salivary gland	- 3/8	- 3.4 – 4.0
- Nerve adjacent to salivary gland	- 4/8	- 0.1 – 0.4

Table 1. Relation between visualized structures.

n.d. = not determined, * = distance between structures too small to measure.

DISCUSSION

Results from the current study demonstrate the potential D-prep MRN can have for further refinement of SPECT/CT-based planning of the SN biopsy procedure in the head-and-neck area. The next step will obviously be to initiate a clinical trial in which D-prep MRN is included in the diagnostic work-up of patients with head-and-neck malignancies that will have to undergo a SN biopsy procedure; such an approach will allow evaluation of the true value of D-prep MRN as well as SPECT and low-dose CT imaging for the SN biopsy procedure within the same patient. We envision that using such a hybrid SPECT/MRI-based approach (Scheme 1), the D-prep MRN findings could potentially provide a more detailed preoperative anatomical atlas with regard to the lymphatic and peripheral nerve anatomy. This feature may in the future help reduce procedure-associated morbidity in the form of nerve damage

Retrospective analysis of patients with head-and-neck malignancies who underwent a SN biopsy procedure indicated that nodal clusters and tumor-positive SNs were most abundantly present in the areas with the most intricate anatomy. This region includes the submandibular region (level IIA and IIB; Scheme 1 and Figures 1-3). Unfortunately more traditional (low-dose) CT-based anatomical reference data failed to detect clustered SNs prior to surgery in up to 15% of cases, which is in agreement with previous studies.[5-8] Furthermore this technique could also not provide feedback regarding the location of the SNs relative to other delicate anatomical structures (e.g. nerves). Based on their similar diffusion properties, the newly introduced D-prep MRN technology allowed clear delineation of LNs and clustered LNs (Figure 2), as well as peripheral nerves (Figure 3). Such visualization may help surgeons to assess variations in both the lymphatic and peripheral nerve anatomy of patients prior to surgery, and adapt their approach accordingly. With a scan time of only a couple of minutes, inclusion of D-prep MRN into the current MRI exam could be rather straight-forward. Further extension of the FOV for D-prep MRN would obviously take longer, but could possibly also enable visualization of other possibly critical structures located in or near level I-V (e.g. the auricular nerve). By also including contrast-enhanced MRI or 3D-time-of-flight (TOF)-based MRI approaches in the MRI protocol, the level of detail in the anatomical atlas could even be increased via the visualization of blood vessels [15, 16]. This can be especially valuable during the resection of cervical SNs in level II, where damage to the accessory nerve is the most significant intraoperative complication [17-19]. Here excision of SNs is hampered by anatomical variances in the course of the accessory nerve (see Figure 3), but also in the location of the nerve as this courses either anteriorly or posteriorly to the internal jugular vein (which occurs in 56% and 44% of patients respectively) [17,20,21].

The concept of preoperative surgical planning is expanding rapidly as it is being combined with (intraoperative) image-guided surgery technologies based on radioactivity-based imaging, fluorescence imaging, and/or a combination thereof [12]. Moreover, navigation technologies, in which surgical tools are navigated in preoperative imaging information [22,23], seems to provide a promising field as it can act as a personalized anatomical atlas. Combined, this refined approach may help to improve intraoperative SN excision, and as such help to reduce the false-negative rates. Although the SN-based application provides a good proof-of-concept application for new surgical guidance technologies, improved visualization of the important anatomical structures present in the surgical field and subsequently, improved surgical planning is certainly not limited to these procedures, or applications in the head-and-neck area for that matter. In our view an obvious extended application of the D-prep MRN technology lies within the virtual planning of oncological surgery where it can complement tumor delineation techniques using radiotracers. This can be particularly valuable in hybrid set-ups such as SPECT/MRI and/or positron emission tomography (PET)/ MRI. One may, for example, reason that overlays of 18F-FDG PET and D-Prep MRN images would enable assessment of the location of critical anatomical structures in relation to the location of the primary tumor. As such these combined images may help to improve the preoperative assessment of the potential nerve damage induced during tumor resection.

Alternatively, application of this approach may also be found in high-precision radiation therapy with intensity-modulated radiation therapy (IMRT), volumetric arc therapy (VMAT) or proton beam therapy. As delineation of target volumes and organs at risk are a major source of uncertainty, and MRI and PET/CT are already increasingly used for this purpose [25]. By including dose constraints to the nerves, sparing may be achieved, reducing treatment-related side effects.

CONCLUSION

The potential of D-prep MRN to provide accurate personalized delineation of LNs and their surrounding delicate anatomies, suggests that that this imaging method may provide a valuable extension of nuclear medicine-based treatment planning technologies. Such a technological evolution is well in line with the ongoing efforts wherein findings at nuclear medicine are linked to state-of-the-art radiological imaging.

11

REFERENCES

1. Mariani G, Erba P, Manca G, Villa G, Gipponi M, Boni G, et al. Radioguided sentinel lymph node biopsy in patients with malignant cutaneous melanoma: the nuclear medicine contribution. J Surg Oncol. 2004;85:141-51.

2. Mariani G, Erba P, Villa G, Gipponi M, Manca G, Boni G, et al. Lymphoscintigraphic and intraoperative detection of the sentinel lymph node in breast cancer patients: the nuclear medicine perspective. J Surg Oncol. 2004;85:112-22.

3. Park SH, Esquenazi Y, Kline DG, Kim DH. Surgical outcomes of 156 spinal accessory nerve injuries caused by lymph node biopsy procedures. J Neurosurg Spine. 2015;23:518-25.

4. van den Berg NS, Brouwer OR, Schaafsma BE, Matheron HM, Klop WM, Balm AJ, et al. Multimodal Surgical Guidance during Sentinel Node Biopsy for Melanoma: Combined Gamma Tracing and Fluorescence Imaging of the Sentinel Node through Use of the Hybrid Tracer Indocyanine Green-(99m)Tc-Nanocolloid. Radiology. 2015;275:521-9.

5. Veenstra HJ, Klop WM, Speijers MJ, Lohuis PJ, Nieweg OE, Hoekstra HJ, et al. Lymphatic drainage patterns from melanomas on the shoulder or upper trunk to cervical lymph nodes and implications for the extent of neck dissection. Ann Surg Oncol. 2012;19:3906-12.

6. Veenstra HJ, Vermeeren L, Olmos RA, Nieweg OE. The additional value of lymphatic mapping with routine SPECT/CT in unselected patients with clinically localized melanoma. Ann Surg Oncol. 2012;19:1018-23.

7. Klop WM, Veenstra HJ, Vermeeren L, Nieweg OE, Balm AJ, Lohuis PJ. Assessment of lymphatic drainage patterns and implications for the extent of neck dissection in head and neck melanoma patients. J Surg Oncol. 2011;103:756-60.

8. Abraham J. Imaging for head and neck cancer. Surg Oncol Clin N Am. 2015;24:455-71.

9. Partovi S, Kohan A, Rubbert C, Vercher-Conejero JL, Gaeta C, Yuh R, et al. Clinical oncologic applications of PET/MRI: a new horizon. Am J Nucl Med Mol Imaging. 2014;4:202-12.

10. Queiroz MA, Huellner MW. PET/MR in cancers of the head and neck. Semin Nucl Med. 2015;45:248-65.

11. Yoneyama M, Takahara T, Kwee TC, Nakamura M, Tabuchi T. Rapid high resolution MR neurography with a diffusion-weighted pre-pulse. Magn Reson Med Sci. 2013;12:111-9.

12. van den Berg NS, Brouwer OR, Klop WM, Karakullukcu B, Zuur CL, Tan IB, et al. Concomitant radio- and fluorescence-guided sentinel lymph node biopsy in squamous cell carcinoma of the oral cavity using ICG-(99m)Tc-nanocolloid. Eur J Nucl Med Mol Imaging. 2012;39:1128-36.

13. Edge SB, Compton CC. The American Joint Committee on Cancer: the 7th edition of the AJCC cancer staging manual and the future of TNM. Ann Surg Oncol. 2010;17:1471-4.

14. Buckle T, van Berg NS, Kuil J, Bunschoten A, Oldenburg J, Borowsky AD, et al. Non-invasive longitudinal imaging of tumor progression using an (111)indium labeled CXCR4 peptide antagonist. Am J Nucl Med Mol Imaging. 2012;2:99-109.

15. Fellner FA, Fellner C, Wutke R, Lang W, Laub G, Schmidt M, et al. Fluoroscopically triggered contrast-enhanced 3D MR DSA and 3D time-of-flight turbo MRA of the carotid arteries: first clinical experiences in correlation with ultrasound, x-ray angiography, and endarterectomy findings. Magn Reson Imaging. 2000;18:575-85.

16. van den Berg R, Verbist BM, Mertens BJ, van der Mey AG, van Buchem MA. Head and neck paragangliomas: improved tumor detection using contrast-enhanced 3D time-of-flight MR angiography as compared with fat-suppressed MR imaging techniques. AJNR Am J Neuroradiol. 2004;25:863-70.

17. Cooper JS, Mukherji SK, Toledano AY, Beldon C, Schmalfuss IM, Amdur R, et al. An evaluation of the variability of tumor-shape definition derived by experienced observers from CT images of supraglottic carcinomas (ACRIN protocol 6658). Int J Radiat Oncol Biol Phys. 2007;67:972-5.

18. Nason RW, Abdulrauf BM, Stranc MF. The anatomy of the accessory nerve and cervical lymph node biopsy. Am J Surg. 2000;180:241-3.

19. Lloyd S. Accessory nerve: anatomy and surgical identification. J Laryngol Otol. 2007;121:1118-25.

20. Lanisnik B, Zargi M, Rodi Z. Electrophysiologic analysis of injury to cranial nerve XI during neck dissection. Head Neck. 2015. doi:10.1002/hed.24002.21.

21. Kim DH, Cho YJ, Tiel RL, Kline DG. Surgical outcomes of 111 spinal accessory nerve injuries. Neurosurgery. 2003;53:1106-12; discussion 2-3.

22. Brouwer OR, Buckle T, Bunschoten A, Kuil J, Vahrmeijer AL, Wendler T, et al. Image navigation as a means to expand the boundaries of fluorescence-guided surgery. Phys Med Biol. 2012;57:3123-36.

23. Zaknun JJ, Giammarile F, Olmos RA, Vidal-Sicart S, Mariani G. Changing paradigms in radioguided surgery and intraoperative imaging: the GOSTT concept. Eur J Nucl Med Mol Imaging. 2012 Jan;39(1):1-3.

24. Bhatnagar P, Subesinghe M, Patel C, Prestwich R, Scarsbrook AF. Functional imaging for radiation treatment planning, response assessment, and adaptive therapy in head and neck cancer. Radiographics. 2013;33:1909-29.

25. Saito T, Ishikawa H, Ohnishi K, Aihara T, Mizumoto M, Fukumitsu N, et al. Proton beam therapy for locally advanced and unresectable (T4bN0M0) squamous cell carcinoma of the ethmoid sinus: A report of seven cases and a literature review. Oncol Lett. 2015;10:201-5.

11

RESULTS

Preoperative identification of SNs using SPECT/CT imaging

A typical example of a SPECT/CT image is provided in Figure SI1. The overlay of CT and SPECT images shown in Figure SI1B, and the 3D volume rendering of these SPECT/CT images (Figure SI1C) enable distinction between the injection site (I) and the SNs (S). Retrospective assessment of SPECT/CT scans of the 140 included patients revealed that of the total number of preoperatively identified SNs (n= 345; Figure SI1D), 79.9% were located in level IB, II and III (283 nodes). Within these three levels, level IIA clearly showed the highest SN incidence (Figure SI1D, highlighted in orange); the number of SNs that were located in level IIA was (over) two-fold higher (120 nodes, 33.8%) than the number of SNs located in level IB (60 nodes, 16.9%), level IIB (53 nodes, 14.9%) or level III (50 nodes, 14.1%).
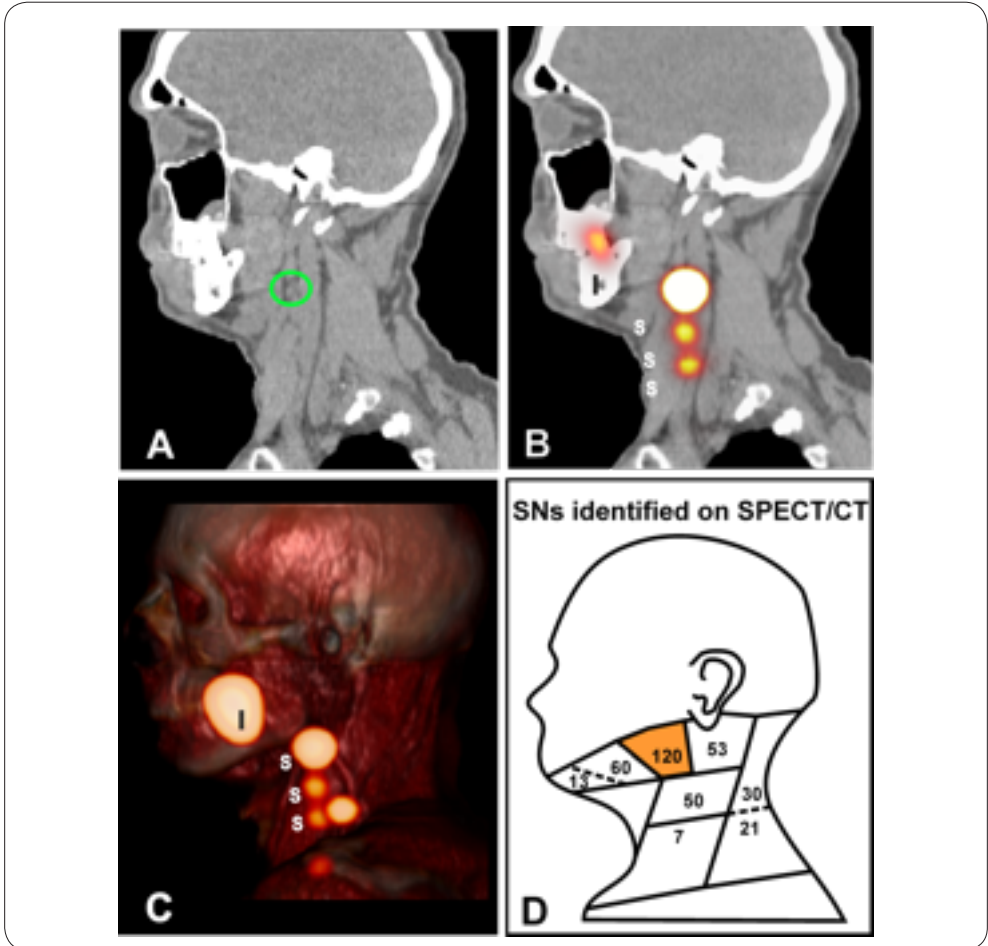
Figure SI1. Preoperative identification of SNs using SPECT/CT imaging.

Preoperative images of a typical patient showing A) a representative CT image with a LN cluster encircled in green, B) a fused SPECT and CT image; and C) a 3D volume rendered SPECT/CT image in which the injection site (I) and identified SNs (S) have been denoted. D) The total number of SNs identified on SPECT/CT in the database containing 140 patients with head-and-neck malignancies, specified per level. The level with the highest number of identified SNs (level IIA) is highlighted in orange.

11

Surgical and pathological findings

In 15% of patients more than one LN was found at the location of the hotspot that was identified as the SN on SPECT/CT. Intraoperatively, 148 nodal clusters were identified, using radioguidance and/or fluorescence imaging (Figure 1). Pathological analysis revealed 21 additional nodal clusters (Figure 1).

The number of SNs excised during surgery was highest in level IIA (37%). At pathology level IIA was also shown to be the level that showed the highest incidence SN metastases was found (42.6%; overall 11.7% of SNs identified in this level contained metastases; Figure 1).

Size lymph nodes and lymph node clusters

Besides defining differences in the lymphatic anatomy (Figure 2), a broad range in LN size could be derived from the MRN images. The mean size of the individual LNs was 100 ± 97 mm3, ranging from small LNs of 21 mm^3 in size to large LNs of 372 mm^3. LN clusters containing up to five nodes measured up to 1233 mm^3. The size of the LNs was also related to the level in which they were located (See Scheme 1 for an overview of the different levels), with the largest LNs identified in level II and III, and the smallest in level IB and IIA (Figure 2; traced in red).

Visualization of nerves and anatomical variances between the position of facial nerves and the submandibular salivary gland

When focusing on the position of facial nerves (Figure 3, in yellow; measured diameter: 1.7-1.9 ± 0.1 mm)) and its marginal mandibular branch another distinct variation was observed. In all subjects the course of the nerves relative to other structures present in the FOV, such as the submandibular salivary gland (S), was also shown to vary. In three subjects the nerve was clearly located alongside to the salivary gland (Figure 3C; distance: 3.6 ± 0.4), while in four others it was located exactly adjacent to the salivary gland (example shown in Figure 3B; distance: 2.3 ± 1.4). In a different volunteer yet another pattern was seen (Figure 3D). The smallest nerve that could be accurately detected was <0.7 mm in diameter. Visualization of the nerves seemed to be related to the angulation of the FOV along the position of the jawbone (planning of the sequence was based on the survey images obtained at the start of the imaging session and the T1-3D TSE reference images). The submandibular salivary gland was detected in all subjects (Table 1).

11